Investigation and Optimization of Textured Water-lubricated Journal Bearings Using Multi-objective Optimization

Q. Li[†], Y. Wang, X. Li, X. Li, G. Zhang, Y. Du and W. Xu

College of New Energy, China University of Petroleum (East China) , Qingdao, China

†*Corresponding Author Email: liq@upc.edu.cn*

ABSTRACT

Water lubricated bearings can be used to reduce contamination due to lubricant leakage in heavy machinery such as power positioning systems of offshore platforms and ship propulsion systems. The lubrication model of a textured two-dimensional parallel friction pair and a textured water-lubricated journal bearing are developed to investigate the lubrication performance. The governing equation is solved, and the fluid cavitation is analyzed using the Zwart-Gerber-Belamri (ZGB) model. A multi-objective optimization method combining the response surface and Non-dominated Sorting Genetic Algorithm-II (NSGA-II) is used to optimize the textured journal bearings. The results indicate that a small texture width will inhibit the occurrence of liquid film cavitation. With the rise in the texture width, the cavitation effect gradually rises and stabilizes. As the texture depth deepens, the micro dynamic pressure effect is enhanced and liquid film pressure rises. Through the tests, it is found that the optimized texture parameters can be implemented to effectively diminish the friction and wear volume, also the optimized textured bearing hydrodynamic pressure effect is enhanced at the same speed.

1. INTRODUCTION

As an important part of supporting the normal operation of rotating machinery, journal bearings are widely used in vessels, submarines and other machinery. The bearing performance will affect the safety and reliability of related equipment. Traditional bearings are generally lubricated with a large amount of oil. In addition, it is necessary to use a good sealing system to prevent the leakage of lubricating oil, which can cause environmental pollution and ecological damage. With the rise in international environmental awareness, the use of water lubrication has become a research hotspot in the field of bearing lubrication (Wang et al., 2016; Qiao et al., 2022; Xie et al., 2023). As a crucial part of the dynamic positioning system of marine propulsion systems, the water-lubricated bearing has changed the status quo of mineral oil as a lubricating medium for a long time, and effectively avoided the serious pollution of the marine environment caused by mineral oil seal leakage. In the meantime, water-lubricated bearings are used in semi-submersible offshore drilling platforms, LNG vessels, submarines and other large marine equipment (Ye et al., 2014, 2016; Zou et al., 2016) because of their wide range

of sources, energy saving and environmental protection (Wang et al., 2003; Guo et al., 2007; Gao et al., 2014). Compared with lubricating oil, a low viscosity lubricating—water leads to a diminution in the load carrying capacity of bearings (Zhou, 2013; Savio et al., 2018; Mallya et al., 2016; Tan 2007), making it impossible to form an effective liquid film between the shaft and the bearing under heavy loads at low speeds. Specifically, the poor load carrying capacity and high friction of water lubricated bearings can have a serious impact on the safety of the power system (Wu et al., 2020). For this reason, surface texture technology has been implemented in water-lubricated bearings. By introducing special surface structures (such as dispersed pits), it is possible to effectively accommodate abrasive chips and rise the load-carrying capacity (Kango et al., 2012; Xiang, 2017; Xi-Jun et al., 2018; Brizmer et al., 2003; Etsion et al., 2004). Therefore, textured water-lubricated bearings have broad application prospects in mechanical devices, especially in ship propulsion systems.

The optimization of texture distribution characteristics has received much attention in earlier studies due to its significant effect on friction (Marian et al., 2007). Marian et al. (2011) found through extensive

NOMENCLATURE			
v_m	mass-average velocity	M_s	solid mass matrix
ρ_m	mixed phase density	C_s	damping matrix
μ_m	fluid viscosity	K_s	stiffness matrix
P	pressure of fluid	r_s	solid displacement
S_v	external force	τ_s	stress on the solid
α_k	volume fraction of kth phase	n	normal vector of the intersection
f	mass fraction of vapor phase	r_f	fluid displacement
R_e	steam production rate	τ_f	stress on the fluid
R_c	steam dissolution rate		

texture test studies that local textures perform better than total textures. As a result, the study of new forms of distribution has been widely emphasized by the academic community. Ji et al. (2021) determined that the convergence ratio and texture parameters affect the load-carrying capacities of bearings by analyzing the effect of local micro-pit textures on the lubricant film pressure distribution of the pad under different convergence ratios.

With the development of surface texture fabrication techniques, it becomes possible to fabricate microstructures with different geometries, which further promotes the development of texture optimization techniques (Gherca et al., 2013). At the same time, many texture design parameters have brought about many design challenges (Gropper et al., 2016). To improve the wear resistance of 45 steel, Guo (2023) machined circular craters at 7%, 14% and 21% on the surface of a friction subsurface and used a universal friction and wear tester to conduct wear resistance tests. Zhao et al. (2020) found that the wear of non-textured surfaces is much greater than that of micro- textured surfaces and determined that the axial distribution of textures has the greatest wear reduction effect according to measurements of the surface moments of friction pairs. Rao et al. (2014) established a theoretical model of coupled stress fluid lubrication for sliding bearings with partial micro-textures using narrow groove theory, analyzed the effects of micro-textures under different depths, lengths, and occupied area ratios.

In summary, the current research on surface texture optimization is relatively limited and needs to be further developed. Factors such as the dimension of the surface texture have a large effect on the lubrication performance. In this study, the influences of texture parameters on the lubrication performance of water-lubricated bearings are studied. With the largest load-carrying capacity and the lowest as the objectives, a multi-objective optimization method combining the response surface and NSGA-II is used to optimize textured journal bearings. Finally, through frictional wear tests and water film pressure tests, it was observed that the optimized texture parameters can effectively lessen the friction and wear volume, and hydrodynamic pressure effect of the optimized textured bearing is enhanced at the same speed. In this paper, the variation law of surface texture parameters and lubrication properties is explored, and its internal mechanism is explained to provide a theoretical foundation for the optimal design of surface textures.

2. NUMERICAL METHOD

2.1 Governing Equations

In this study, thermal effect is ignored. The lubricant, water, has a constant viscosity and density. The surface deformation is negligible. The basic flow governing equations, are given as follows:

$$\frac{\partial}{\partial t}(\rho_m) + \nabla \cdot (\rho_m \boldsymbol{v}_m) = 0 \tag{1}$$

$$\frac{\partial}{\partial t}(\rho_m \boldsymbol{v}_m) + \nabla \cdot (\rho_m \boldsymbol{v}_m \boldsymbol{v}_m) = \nabla \cdot \left[\mu_m (\nabla \boldsymbol{v}_m + \nabla \boldsymbol{v}_m{}^T) \right] - \nabla p + S_v \tag{2}$$

where v_m and ρ_m can be expressed as follows:

$$\boldsymbol{v}_m = \frac{\sum_{k=1}^{n} \alpha_k \rho_k \boldsymbol{v}_k}{\rho_m} \tag{3}$$

$$\rho_m = \sum_{k=1}^{n} \alpha_k \rho_k \tag{4}$$

The lubrication flow field in water-lubricated bearings is a two-phase flow when the cavitation phenomenon caused by the texture inlet and bearing divergence wedge is considered. In this paper, the Mixture model is chosen to simulate the cavitation phenomenon. The volume fraction of the gas α_k can be calculated by the vapor transport equation (ANSYS, 2011) in Equation (5) as follows:

$$\frac{\partial}{\partial t}(\rho_m f) + \nabla (\rho_m \boldsymbol{v}_m f) = \nabla (\mu_m \nabla f) + R_e - R_c \tag{5}$$

In this study, the ZGB cavitation model proposed by Dobrica et al., (2010) is used with the following expressions:

$$\begin{cases} R_e = F_{vap} \dfrac{3\alpha_{nuc}(1-\alpha_v)\rho_v}{R_B} \sqrt{\dfrac{2}{3}\dfrac{(p_v - p)}{\rho_l}} & p \le p_v \\[3mm] R_c = F_{cond} \dfrac{3\alpha_v \rho_v}{R_B} \sqrt{\dfrac{2}{3}\dfrac{(p - p_v)}{\rho_l}} & p > p_v \end{cases} \tag{6}$$

where F_{vap} is the evaporation coefficient, and F_{cond} is the coefficient of condensation., usually take $F_{vap} = 50$, $F_{cond} = 0.01$.

2.2 Multi-Objective Optimization Model

The design of experiments (DOE) and response surface optimization (Wang, 2021) is chosen for this
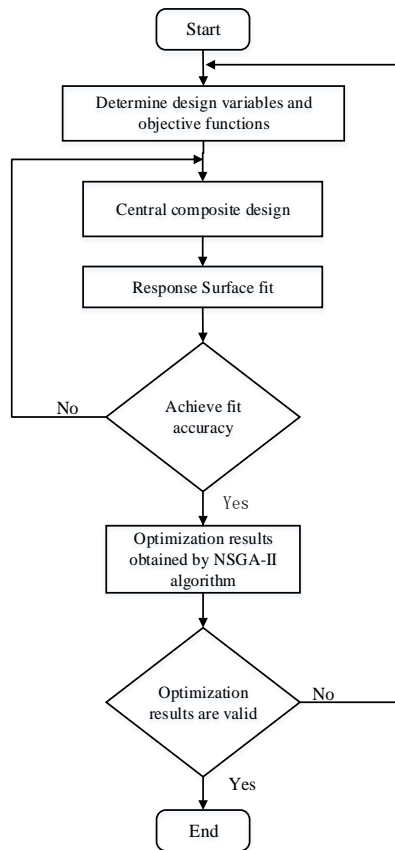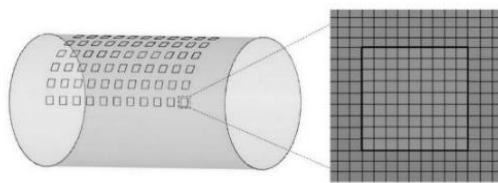
Fig. 1 Flow chart of the optimization design

Fig. 2 Structure of the 3D textured journal bearing and mesh of the textures

Table 1 Main parameters of the calculation model

Symbol	Parameter	Value
Structural parameters of journal bearing		
L_0/mm	Length of journal bearing	80
D/mm	Diameter of journal bearing	160
e	Eccentricity	0.6
Structural parameters of single texture		
d/mm	the texture width	4
h/mm	the texture depth	3
h_0/mm	the film thickness	1.5
L/mm	the length of single texture	8
Lubricating medium parameters		
ρ_l/kg/m^3	Density of liquid phase water	998.2
μ_l/Pa•s	Viscosity of liquid phase water	1×10^{-3}
ρ_g/kg/m^3	Density of vapor phase water	0.5542
μ_g/Pa•s	Viscosity of vapor phase water	1.34×10^{-5}
p_v/Pa	Saturated water vapor pressure	3540
Boundary conditions		
v/(m·s^{-1})	sliding speed	50
P_{in}/Pa	Inlet pressure	0
P_{out}/Pa	Outlet pressure	0
P_{ope}/Pa	Environment pressure	101325

The two-dimensional textured configuration of the parallel contact pair model is shown in Fig. 3. When h/d = 0.75, d/L = 0.5, h/h_0 = 2, the structural parameters are shown in Table 1. Periodic boundary conditions are considered at the left and right inlets and outlets. The upper wall slides from left to right with a velocity v, while the no-slip boundary condition is adopted. The remaining walls have fixed boundary conditions.
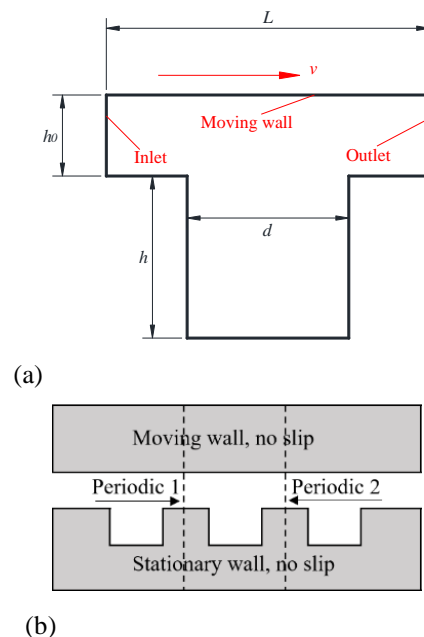
research to build the optimization system. Then, the problem is solved using NSGA-II. In this study, the central composite design (CCD) approach is used for the DOE. A flowchart of the optimization system(Deb et al., 2002; Ilka et al., 2018; Wang et al., 2018) is shown in Fig. 1.

2.3 Physical Model

The three-dimensional textured configuration model is shown in Fig. 2. Based on a cylindrical radial plain bearing, the lubricating medium enters the bearing gap from one end and exits from the other end. Among all the shapes studied, the square shaped bottom profile has been shown to offer the best tribological performance (Uddin et al., 2017). Therefore, in this paper, the cross-section of the texture structure is a square. The laminar flow model is selected. The import and export are pressure boundary conditions. The main structural parameters are shown in Table 1. The index v denotes the vapor, l denotes the liquid.

(a)

(b)

Fig. 3 (a) Texture shape (b) Boundary conditions

Table 2 Comparison of loading capacity with different numbers of grids

Mesh number (thousand)	Load-carrying capacity (N)	Rate of change
120	1288.10	—
170	1355.65	4.98%
220	1401.46	3.27%
270	1432.10	2.14%
330	1432.51	0.03%
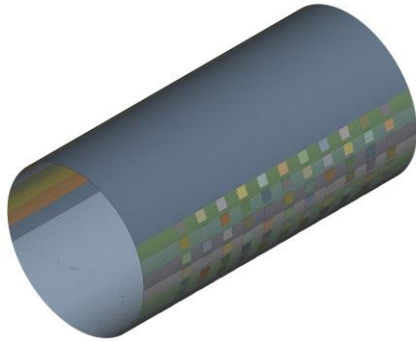
(a) Global grid
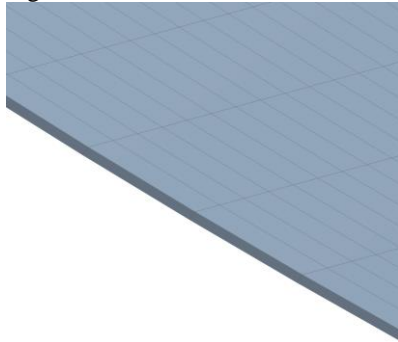
(b) local mesh

Fig. 4 Liquid film meshing diagram

2.4 Mesh

In order to reduce calculation time and running memory and eliminate calculation errors caused by grid division, grid independence verification is carried out. In order to obtain the appropriate number of grids, the number of five groups of grids is selected for calculation, and the load-carrying capacity is selected as the measurement standard. The load-carrying capacity under different grid numbers is shown in Table 2. As can be seen from the table, with the increase of the number of grids, the load-carrying capacity increases, and when the number of grids reaches 270,000, the load-carrying capacity tends to be stable, so the number of grids of 270,000 is finally selected for simulation calculation, in which the liquid film thickness direction is divided into 6 layers, and the final liquid film grid division is shown in Fig. 4.

The governing equations are settled via FLUENT. The finite volume method (Li et al., 2004) is used to decentralized the governing equations. When the continuity equation residuals fall to 1×10^{-4} and the import and export flows are stable and basically equal, the calculation converges. Typically, 20,000 iterations are performed.

2.5 Mechanical Parameters

After calculating the liquid film pressure distribution and fluid shear stress, the pressure on the upper wall is integrated to obtain the liquid film load-carrying capacity(LCC) as follows:

$$LCC = \iint P dx dy \tag{7}$$

where, P is the pressure on the upper wall.

The fluid shear stress in contact with the rotor surface is integrated to obtain the friction force(F_f) of the liquid film acting on the rotor surface as follows:

$$F_f = \iint \tau dx dy \tag{8}$$

where, τ is the fluid shear stress.

3. INFLUENCE OF THE TEXTURE PARAMETERS

3.1 h/d

Figure 5 depicts the variation in the load-carrying capacity with h/d under different d/L and h/h_0. This indicates that the load-carrying capacity rises with h/d under different d/L. However, the load-carrying capacity shows different trends under different h/h_0. When $h/h_0 = 1$, the load-carrying capacity falls first and then rises. In the remaining cases, the load-carrying capacity rises with h/d, and the growth rate rises with increasing of h/h_0.
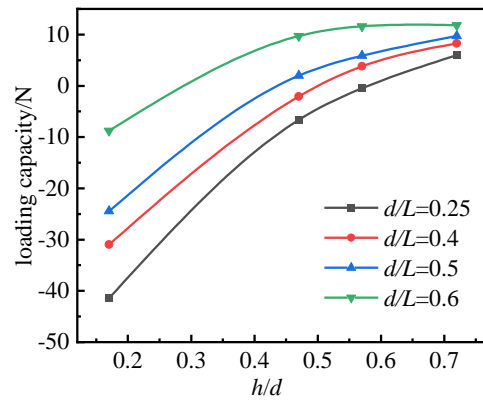
(a) Different d/L
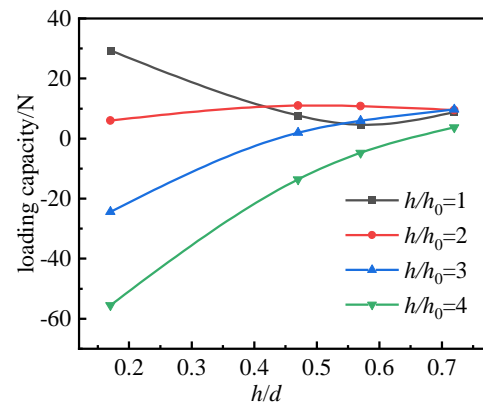
(b) Different h/h_0

Fig. 5 Change in the load-carrying capacity versus h/d
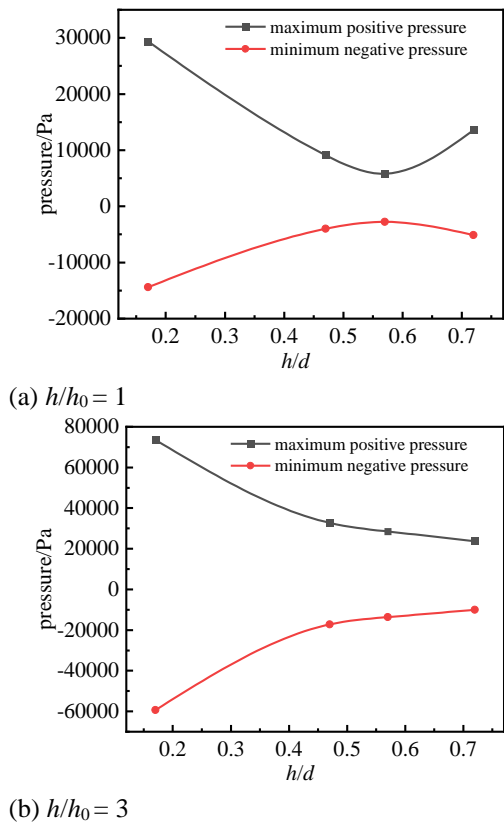
(a) $h/h_0 = 1$

(b) $h/h_0 = 3$

Fig. 6 Change of maximum positive pressure and minimum negative pressure verse h/d

Figure 6 shows the change curves of the maximum positive pressure and minimum negative pressure with h/d under $h/h_0 = 1$ or 3. This figure can also be used to analyze the reasons for the change in the load-carrying capacity
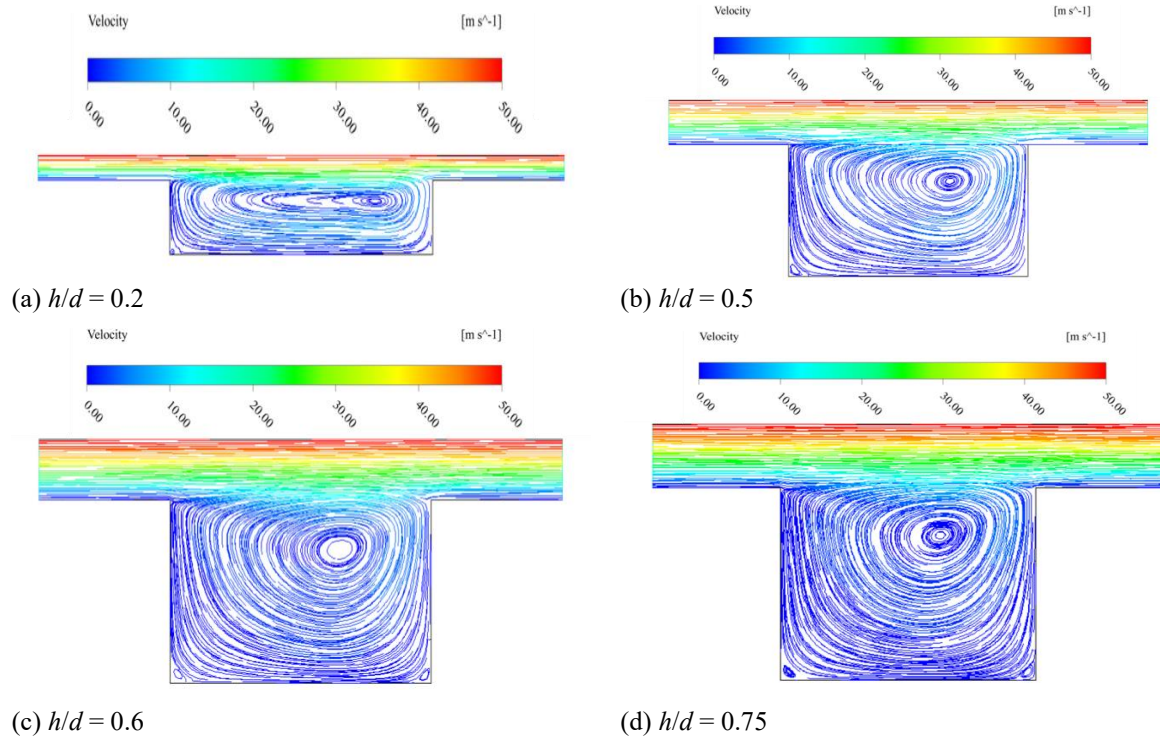
with h/d. The trends of the maximum positive pressure and minimum negative pressure with h/d are basically the same under different h/h_0. This is because the texture depth rises as h/d rises, the flow of the lubricating medium is impeded by the bottom contour of the texture, and the vortex flow inside the texture rises (as shown in Fig. 7). Under the effect of vortex flow inside the texture, the dynamic pressure effect is weakened and the maximum positive pressure falls with increasing h/d.

Figures 8-9 show the pressure distribution contours under different h/d for $h/h_0 = 1$ or 3. As shown in Fig. 8, when $h/h_0 = 1$, with increasing in the h/d, the percentage of the positive pressure area falls. Hence the load-carrying capacity of the frictional pair falls. Figure 9 shows that when $h/h_0 = 3$, the percentage of the negative pressure area falls and the minimum negative pressure rises. Therefore, the load-carrying capacity of the frictional pair rises with h/d.

3.2 d/L

Figure 10 shows the load-carrying capacity curve with d/L under different h/d and h/h_0. As shown in the figure, under different h/d, the load-carrying capacity rises with d/L, and at the same time, the growth rate falls with increasing h/d. The load-carrying capacity shows different trends under different h/h_0, which indicates that the load-carrying capacity is related to the comprehensive selection of each ratio.
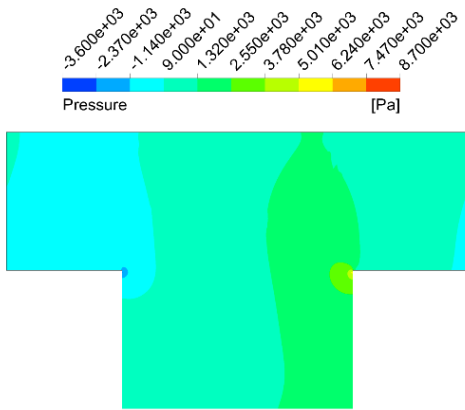
When $h/d = 0.75$ and $h/h_0 = 3$, Fig. 11 shows that at the same h/d and h/h_0, as d/L rises, the maximum positive pressure rises, while the negative pressure area falls, which rises the load-carrying capacity.
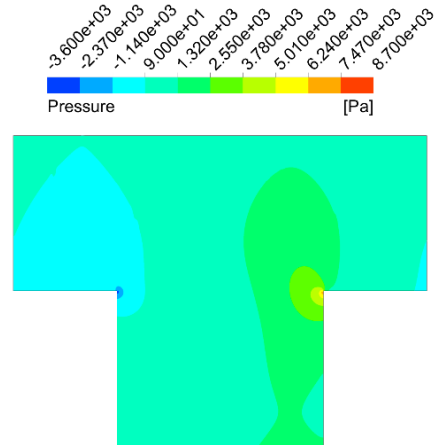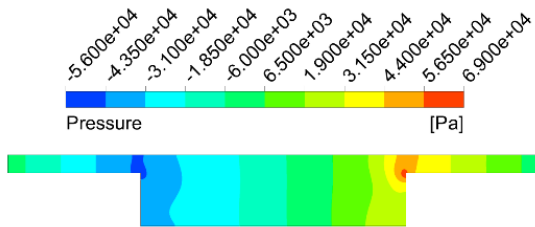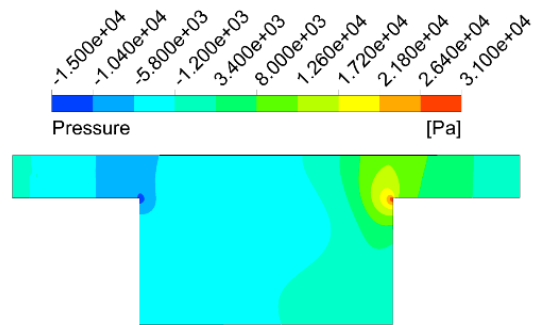

(a) $h/d = 0.2$
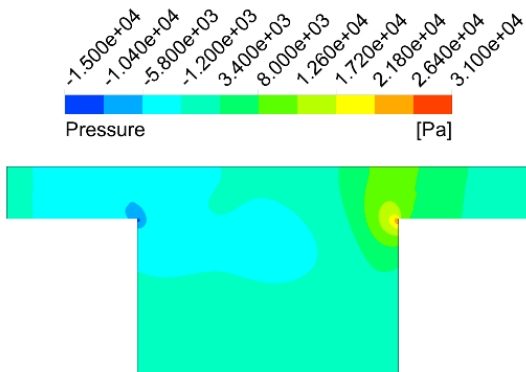

(b) $h/d = 0.5$

(c) $h/d = 0.6$

(d) $h/d = 0.75$

Fig. 7 Velocity Streamline under different h/d
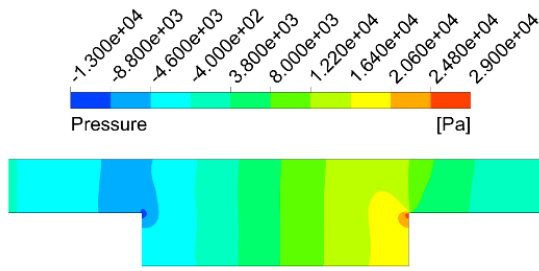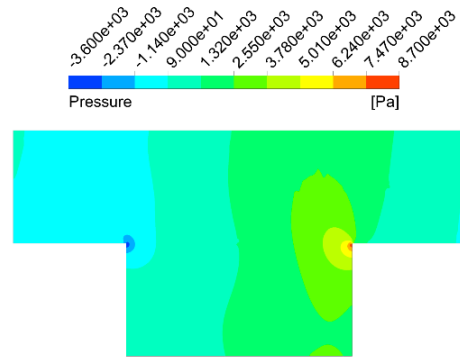
(a) *h*/*d*=0.2

(b) *h*/*d*=0.5

(c) *h*/*d*=0.6

(d) *h*/*d*=0.75

Fig. 8 Pressure distribution contours under different *h*/*d* for *h*/*h*$_0$ = 1

(a) *h*/*d* = 0.2

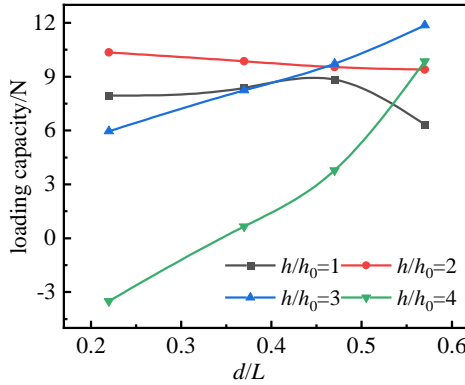(b) *h*/*d* = 0.5

(c) *h*/*d* = 0.6
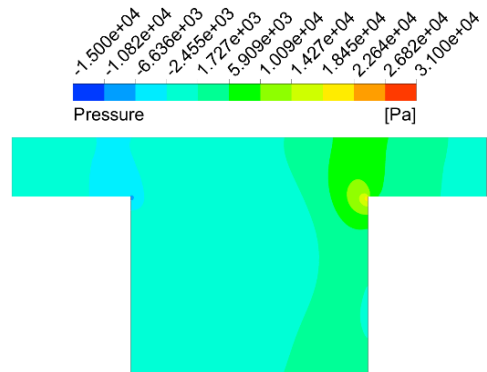
(d) *h*/*d* = 0.75

Fig. 9 Pressure distribution under different *h*/*d* for *h*/*h*$_0$ = 3
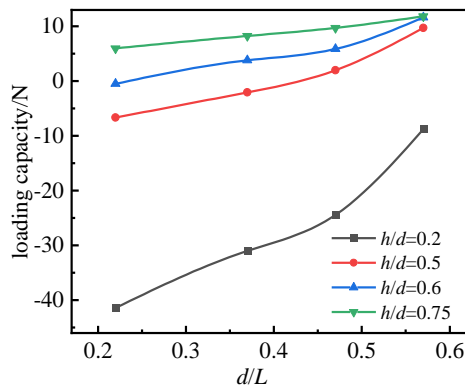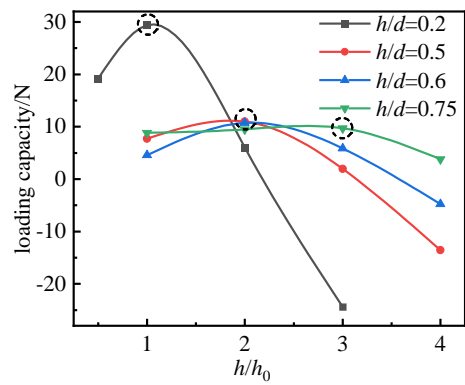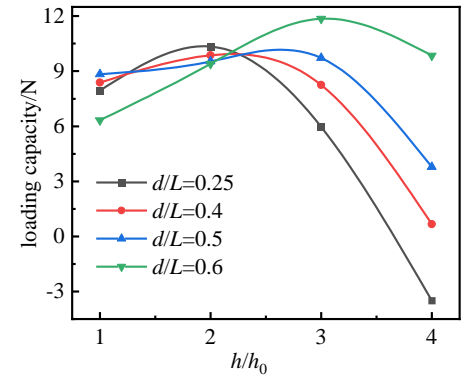
(a) Different *h/d*

(b) Different *h/h₀*

Fig. 10 Change of load-carrying capacity verse *d/L*

(a) Different *h/d*

(b) Different *d/L*

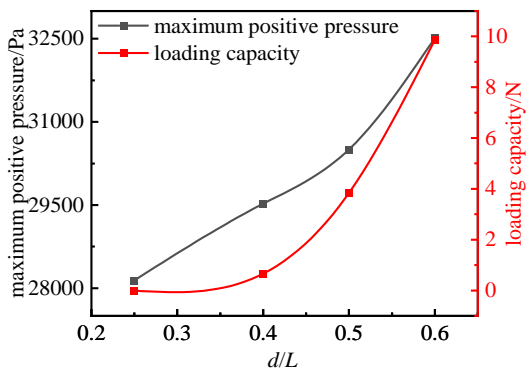**Fig. 12 Change of the load-carrying capacity versus *h/h₀***

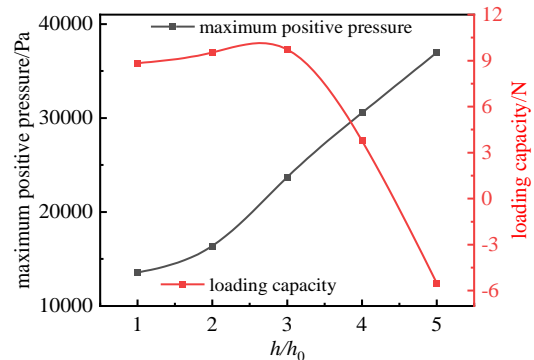**Fig. 11 Changes in the maximum positive pressure and load-carrying capacity versus *d/L***

**Fig. 13 Change in the maximum positive pressure and load-carrying capacity versus *h/h₀***

3.3 *h/h₀*

For different *h/d* and *d/L*, the change trend of the load-carrying capacity with *h/h₀* is the same, increasing first and then decreasing. Therefore, there exists an optimal *h/h₀* to maximize the load-carrying capacity. Figure 12-a demonstrates that the smaller *h/d*, the greater the effect of *h/h₀* on the load-carrying capacity. At the same time, as *h/d* rises, the highest point moves to the right; that is, the optimal *h/h₀* is different under different *h/d* values.

As can be seen from Fig. 13, as h*/h₀* rises, the highest positive pressure rises, and the load-carrying capacity rises accordingly. However, at the same time, the area of the negative pressure zone rises and the minimum negative pressure falls, which bring about a fall in the load carrying capacity.

4. OPTIMAL DESIGN AND TEST VERIFICATION

The effects of texture parameters on lubrication performance of textured journal bearings are analyzed by establishing a three-dimensional textured journal bearing. With the objectives of maximum load-carrying capacity and minimum friction, the dimensional and distribution parameters of textured journal bearings are optimized via NSGA-II, and at the same time, the influences of the texture width, depth, and distribution angle on the lubrication performance of textured journal bearings are analyzed. In this section, the crossover probability of NSGA-II algorithm is set as 0.9, the crossover distribution
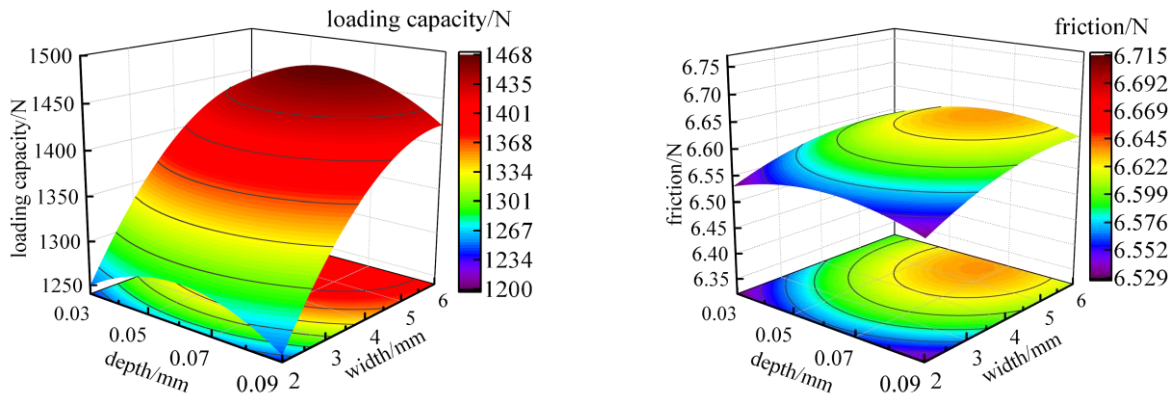
(a) Response relationship between the load-carrying capacity and texture dimension parameters

(b) Response relationship between the friction and texture dimension parameters

Fig. 14 Response relationship between the lubrication performances and texture dimension parameters

index as 20, the mutation probability as 0.1, the variation distribution index as 20, the population number as 200, the iteration algebra as 500, and the Pareto set is obtained. There are constraints on the size variation range of distribution parameters and dimension parameters. Finally, the validity of the optimization results is verified by frictional wear tests and water film pressure tests.

4.1 Optimal Design of the Dimensional Parameters of the Texture

The dimensional of the initial model are: the texture depth is $h = 0.03$ mm and the texture width is $d = 4$ mm. According to the calculation model, the following computational results are obtained: the load-carrying capacity is 1,387.60 N and the friction is 6.6103 N.

The depth and width of the texture are used as design variables. In this paper, central composite design (CCD) is used for the design of experiment (DOE) for the design variables. The CCD, one of the most typical techniques in the design of experiment process, is suitable for calibrating quadratic response models. The load-carrying capacity and friction at each design point are calculated using the corresponding CFD. Then, regression is used to obtain the quadratic polynomial regression equations and response surfaces for the load-carrying capacity and friction. The determination coefficients of the partial F-tests for the target parameters are 0.9958 and 0.9859, respectively, indicating that the generated response surfaces are of high quality. Based on the above analysis, the quadratic polynomial regression equation is as follows:

$$W = 905.6523 + 5003.3957h + 139.7792d \\ -66.2654hd - 40914.6441h^2 - 11.2893d^2 \tag{9}$$

$$f = 6.3348 + 4.2586h + 0.0589d + 0.0822hd \\ -36.5259h^2 - 5.7734 \times 10^{-3}d^2 \tag{10}$$

Figure 14 shows the response surface between each target parameter and the design parameter. As shown in the figure, the load-carrying capacity rises and then falls with an increasing texture depth, while it rises with an increasing texture width. At the same time, the magnitude

of the change in the load-carrying capacity is large, while the variation in friction is small.

Based on the response relationship between the bearing lubrication performance and dimensional parameters, the NSGA-II is utilized to optimize the design of the texture dimensional parameters. The optimized texture dimensions as follow: the texture depth is 0.038 mm and texture width is 5.03 mm.

As can be seen from Fig. 15, the cavitation effect of the bearing is suppressed when the width of the texture is too small. As the width of the texture rises, the cavitation area of the bearing gradually rises and then becomes stable. The cavitation inhibits the pressure reduction in the negative pressure area, thus enlarging the load-carrying capacity.

To analyze the reason for the change in load-carrying capacity along with the texture depth, the circumferential pressure distribution curves under different texture depths are developed. As illustrated in Fig. 16, when the texture depth is too small, the micro-dynamic pressure lubrication effect is not obvious. As the depth of the texture rises, the micro-dynamic pressure effect rises, and consequently the load-carrying capacity rises. When the depth rises to a certain value, the outflow of the lubricating medium is obstructed by the texture profile, which weakens the dynamic pressure effect. Moreover, the lubricant film thickness rises with texture depth, which results in a fall in the total pressure and load carrying capacity of the fluid film. Based on the above analysis, there is an optimal texture depth that maximizes the load-carrying capacity.

4.2 Optimal Design of the Texture Distribution Parameters

To further optimize the lubricating performance of the textured bearings, based on the optimized dimensional parameters, the texture distribution angle $\alpha=-45°$, axial distance $s=10$ mm and circumferential distance $\varphi=15°$ are initially selected to optimize the texture distribution parameters. The angle between the edge of the texture region and the horizontal axis is defined as the texture distribution angle α. To optimize the distribution

(a) *d*=2 mm

(b) *d*=3 mm
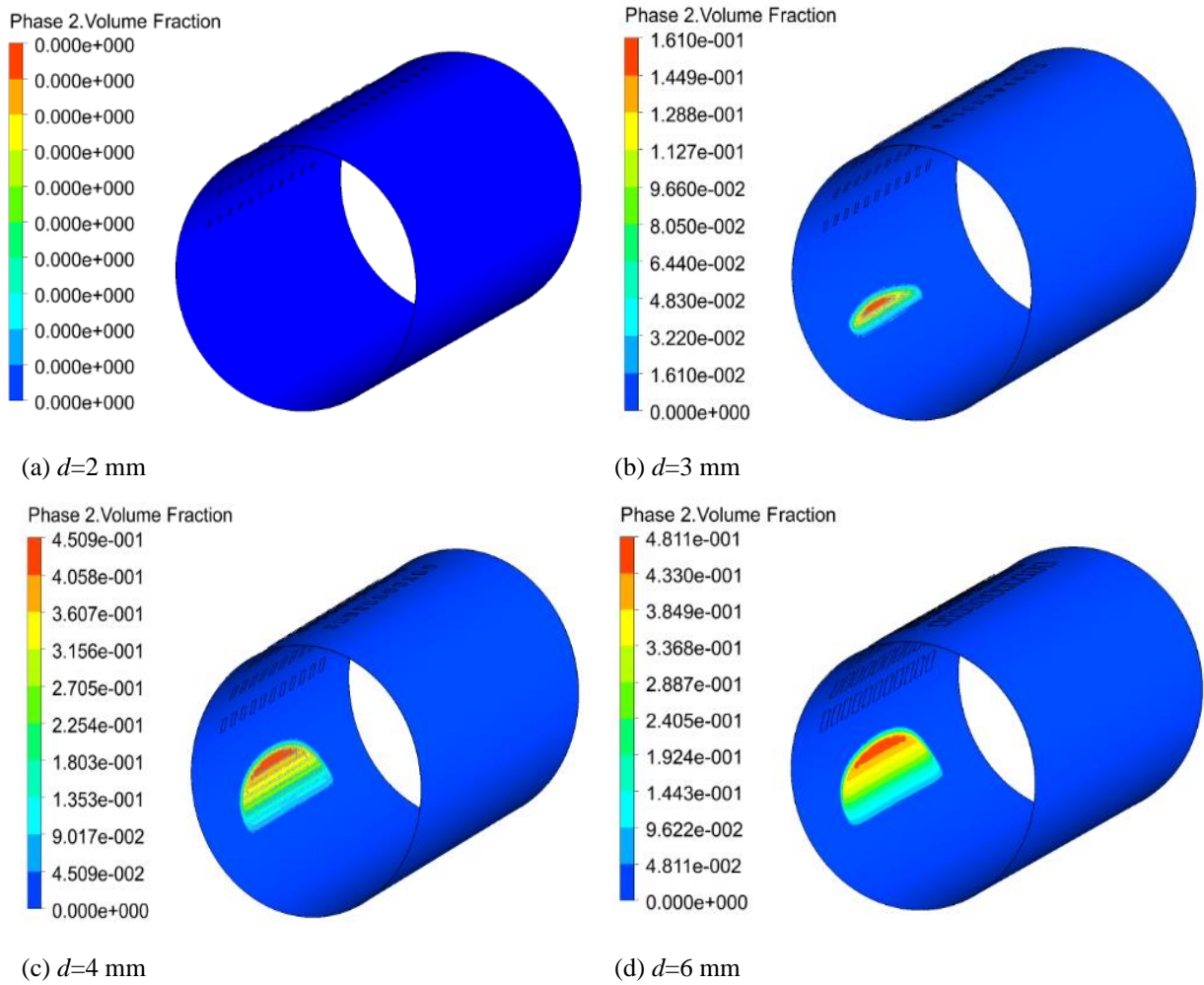
(c) *d*=4 mm

(d) *d*=6 mm

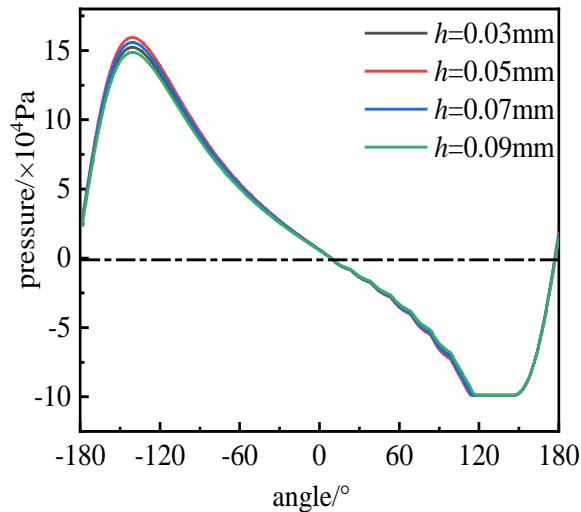**Fig. 15 Gas phase volume fraction contours under different texture widths**

**Fig. 16 Pressure distribution curves for different texture depths**

parameters of the texture, the distribution angle, axial distance and circumferential distance of the texture are used as design variables. The quadratic polynomial regression equation (Equations 11-12) and response surface diagram (Fig. 17) are obtained by using the analysis method in Section 4.1.

$$W = 1315.8266 + 3.2611\alpha + 13.6997s + 2.96527\varphi$$
$$-0.2143\alpha s - 0.0457\alpha\varphi - 1.548s\varphi \qquad (11)$$
$$-5.2122 \times 10^{-3}\alpha^2 + 1.6465s^2 + 0.16576\varphi^2$$

$$f = 7.0297 + 3.7611 \times 10^{-3}\alpha - 0.0413s$$
$$-0.0220\varphi - 3.4777 \times 10^{-4}\alpha s - 7.3780 \times 10^{-5}\alpha\varphi$$
$$-3.4432 \times 10^{-3}s\varphi - 6.5663 \times 10^{-8}\alpha^2 \qquad (12)$$
$$+4.2877 \times 10^{-3}s^2 + 1.6477 \times 10^{-3}\varphi^2$$

Figure 17 shows the response surface between each target parameter and the design parameter. As the design variables change, the magnitude of the change in the load-carrying capacity is large, while the variation in the friction is small. As the distribution angle rises, the load-carrying capacity tends towards to rise and then fall, and the friction shows an overall decreasing trend. As the axial distance rises, there is an overall rise in load-carrying capacity and an overall fall in friction. Both the load-carrying capacity and friction show an overall decreasing trend with an increasing circumferential distance. Based on the response relationship between the bearing lubrication performance and dimensional parameters, the following optimized texture distribution parameters were used: α= 85°, s = 11 mm and φ = 10.2°.
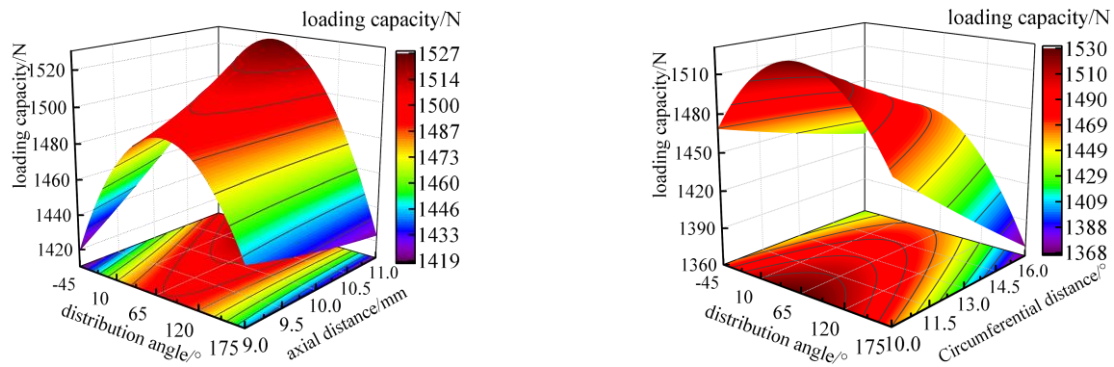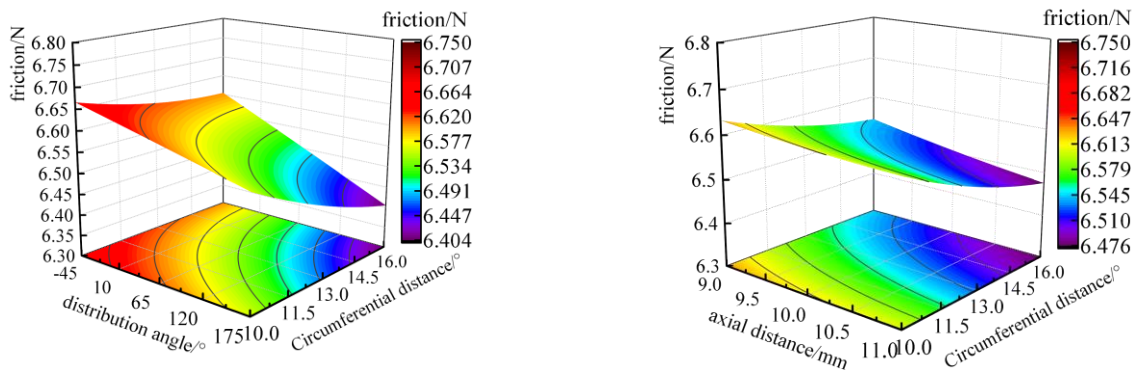
(a) The response relationship among the load-carrying capacity, distribution angle and axial distance

(b) The response relationship among the load-carrying capacity, distribution angle and circumferential distance
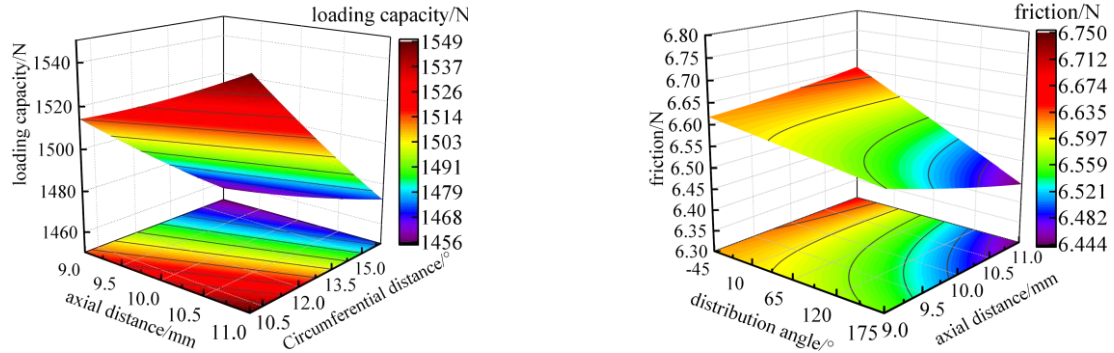
(c) The response relationship among the load-carrying capacity, axial distance and circumferential distance

(d) The response relationship among the friction, distribution angle and axial distance

(e) The response relationship among the friction, distribution angle and circumferential distance

(f) The response relationship among the friction, axial angle and circumferential distance

Fig. 17. Response relationship among the texture distribution parameters, the load-carrying capacity and friction of the textured journal bearing
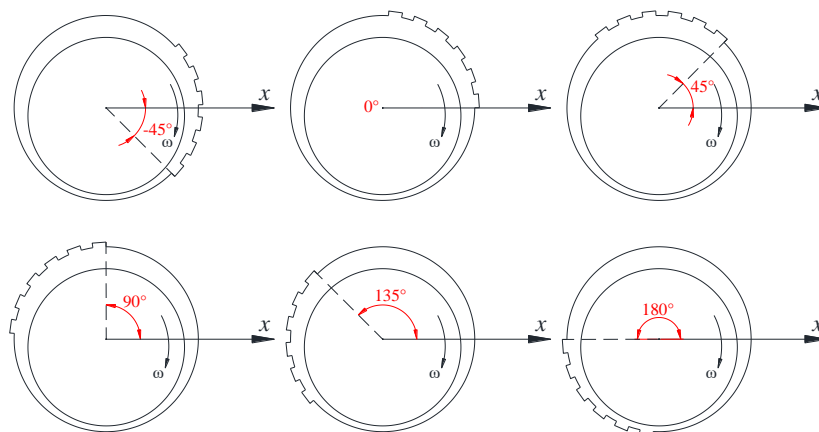

Fig. 18. Diagram of the different texture distribution angles

To analyze the influence of different texture distribution angles on the lubrication performance of textured journal bearings, six different distribution angles are considered, as shown in Fig. 18. The distribution angles are α = -45°, 0°, 45°, 90°, 135° and 180°, and the direction of rotation is counterclockwise. The liquid film pressure contours under different distribution angles are given in Fig. 19. The figure shows that when the texture is situated in the minimum film thickness region, the presence of the texture has a destructive effect on the area of the positive pressure zones (Fig. 19-a) and negative pressure zones (Fig. 19-d) while reducing the maximum film pressure. When the texture is situated near the maximum film gap thickness (Figs 19-b and c), the existence of the texture makes the dynamic pressure effect

more significant and rises the maximum film pressure. Figure 20 shows the gas phase volume fraction contours under different distribution angles. From this, as the distribution angle of the texture rises, the distribution approaches the cavitation region, and the texture disrupts the continuity of cavitation region and forms an interrupted cavitation region.

In summary, the load-carrying capacity rises as texture moves from minimum film thickness region to the maximum film thickness region. The load-carrying capacity falls as the texture moves from the region of maximum film thickness to the region of minimum film thickness of the evanescent wedge.

(a) σ=-45°

(b) σ=45°

(c) σ=90°

(d) σ=180°
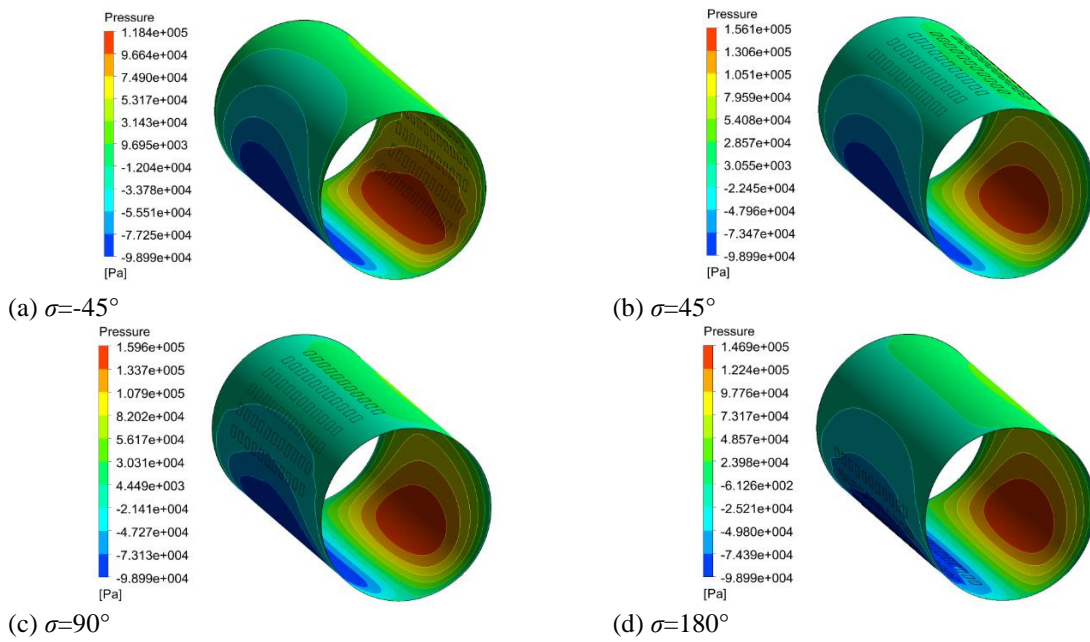
Fig. 19 Liquid film pressure distribution contours under different distribution angles

(a) σ=0°
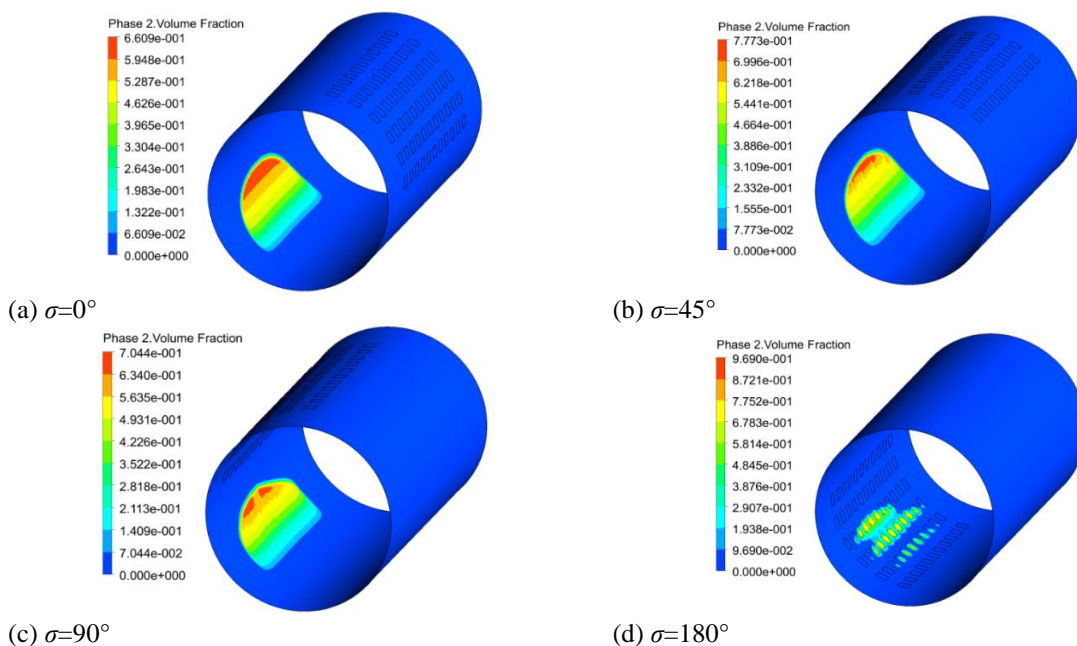
(b) σ=45°

(c) σ=90°

(d) σ=180°

Fig. 20 Gas phase volume fraction contours under different distribution angles
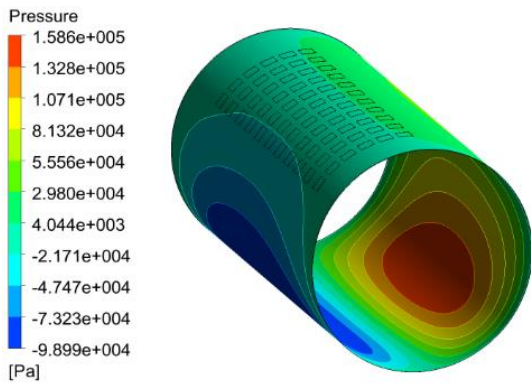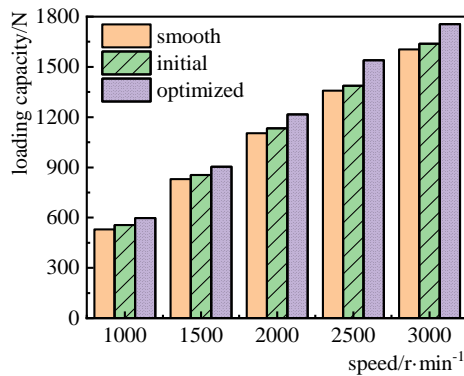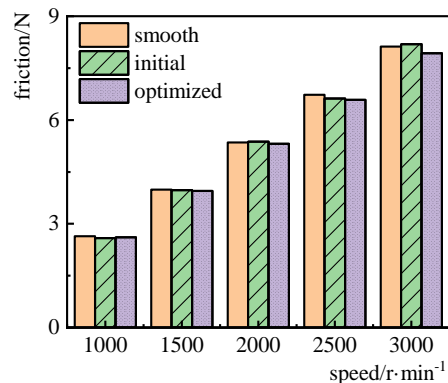
Fig. 21 Liquid film pressure distribution contours under optimized parameters

(a) Load-carrying capacity

(b) Friction

Fig. 22 Comparison of the lubrication performance of different structural journal bearings at different speeds

Based on the above optimized texture distribution parameters, a calculation model of the journal bearing with a texture depth of 0.038 mm, a texture width of 5.03 mm, α of 85°, s of 11 mm and φ of 10.2° is established. The liquid film pressure contour is obtained via simulation, as shown in Fig. 21. The maximum pressure of the liquid film obtained by optimization is improved. Moreover, the optimized load-carrying capacity and friction force are 1530.10 N and 6.5866 N, respectively, and their predicted values are 1539.06 N and 6.5846 N, respectively. The calculated values of the optimized and the predicted values of the model are compared. The error of both models is less than 0.6%, which shows that the model has nice reliability.

The effectiveness of the optimized distribution parameters for improving the lubrication performance of bearing is verified. Figure 22 shows the change in the lubrication performance with speed for the smooth bearing, the initial bearing and the optimized bearing. As shown in the figure, the optimized distribution parameters significantly enhance the lubrication performance. The friction is fallen, and the lubrication performance is improved.

4.3 Test Verification

(1) Frictional properties of friction

An MFT-5000 multi-functional friction and wear tester is utilized to test the wear volume and friction force of the textured friction pair before and after optimization by reciprocating motion.

To facilitate the processing and testing of the surface texture, the size of the texture in the sliding bearing is risen in equal proportions, and a 25 mm × 25 mm nylon material test block with a thickness of 5 mm is used for the lower sample. The surface texture structure is prepared on the surface of the test block by means of CNC machining. Table 4 shows the specific dimensions of the textured structure samples, where Sample 4 is the optimized sample block. Figure 23 shows a picture of the lower sample with the texture after processing, from which it can be seen that the shape of the texture is regular. The upper sample is made of GCr15 bearing steel with a diameter of 6.35 mm. Combining the material properties of the upper and lower samples, the test parameters are shown in Table 5.

Fig. 23. Photo of the sample

Table 4 Parameters of each texture sample

	Texture width/mm	Texture depth /mm
Sample 1	0.6	0.06
Sample 2	0.7	0.06
Sample 3	0.8	0.06
Sample 4	0.8	0.04

Table 5 Test parameters

Test parameters	Value
Indoor temperature/°C	25 ℃
loading/N	10
Itinerary/mm	15
Frequency/Hz	15
Duration/s	1200
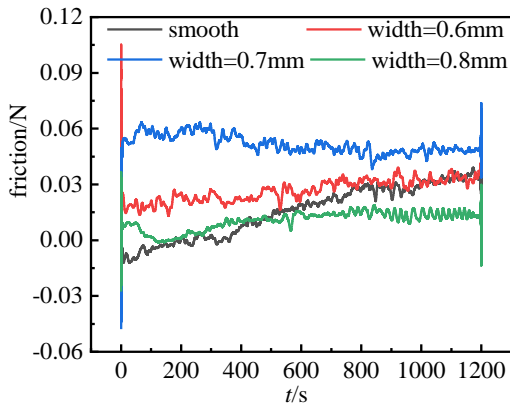
(a) Different texture widths
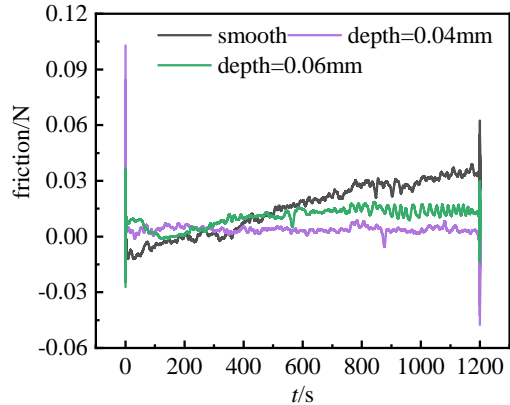
(b) Different texture depths

Fig. 24 Friction curve with time

(a) Smooth

(b) Textured

Fig. 25 Photos of the water-lubricated journal bearings

Table 6 Wear volume of each sample

Samples	Wear volume/mm^3
Smooth	0.050
Sample 1	0.106
Sample 2	0.179
Sample 3	0.046
Sample 4	0.041

The variation curves of friction with time for different texture widths and different texture depths are given in Fig. 24. As can be seen in the figure that a reasonable texture parameter can effectively reduce the sample friction compared with the smooth sample. However, when the width of the texture is too large, the friction of the sample will rise. The test demonstrated that the friction rose and then fell with the texture width at the same texture depth, which is consistent with the theoretical research results. Among them, sample 4 has significantly lower friction than the smooth samples and other samples. The wear volumes of the five samples are shown in Table 6. The wear volume of sample 4 is reduced by 18% compared with that of the smooth sample. The wear volume of sample 4 is reduced to different degrees compared with that of the other samples. This proves that the optimized texture parameters have a good wear reduction effect.

(2) Liquid film pressure

To validate the effectiveness of the optimization results, based on the existing journal bearing test bench in the laboratory (Zhang, 2020), the optimized textured bearing and smooth bearing water film pressures are tested and compared.

To gauge the unceasing pressure distribution in the circumferential, radial and axial diversion holes were machined on the spindle (as shown in Figs 26-a and b) and diversion slip rings were installed (as shown in Fig. 26-c). The liquid film pressure is extracted. Finally, a pressure sensor (as shown in Fig. 26-d) is installed to gauge the pressure distribution in the circular orientations.

Figure 25-a shows that the smooth bearing is made of nylon. The hole on the top of the bearing is a positioning hole for preventing the bearing from rotating during the test. The optimized texture depth of the textured journal bearing is 0.038 mm. However, processing technology such as 3D printing is not sufficiently accurate. Therefore, a laser process is used to process a square textured structure with a thickness of 0.04 mm. As shown in Fig. 25-b, the film is then bonded to the inner surface of the bearing to achieve high precision in the fabrication of the textured journal bearing.

Water film pressure tests were conducted on smooth bearings and optimized textured bearings. To ensure the reliability of the data, a simulation calculation of the liquid film pressure of the textured journal bearing at 800 r·min^{-1} was carried out. A comparison of the calculation and test results is shown in Fig. 27, where the water film pressure changes in the same trend.
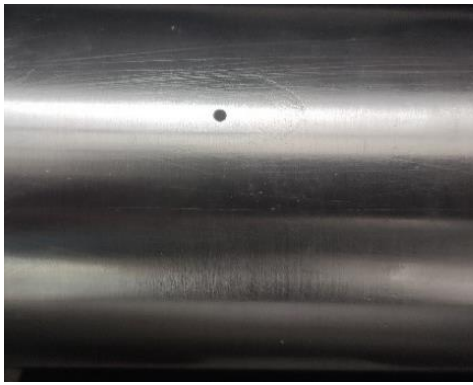
(a) Radial diversion hole

(b) Axial diversion hole
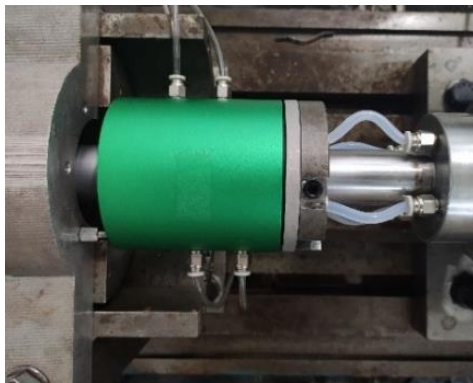
(c) Diversion slip ring and diversion pipe

(d) Pressure sensor

Fig. 26 Pressure test system

Fig. 27 Comparison of the water film pressures between the test and simulation results

(a) (N=600 r·min⁻¹)

(b) (N=800 r·min⁻¹)

(c) (N=1000 r·min⁻¹)

Fig. 28 Comparison of the water film pressure between smooth and textured journal bearings

Figure 28 shows a comparison of the water film pressures of smooth and textured journal bearings at speeds of 600 r·min⁻¹, 800 r·min⁻¹ and 1000 r·min⁻¹. From
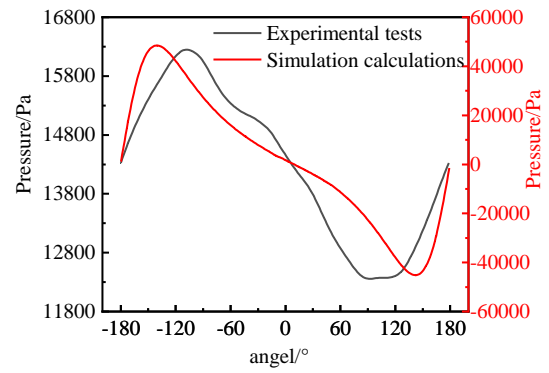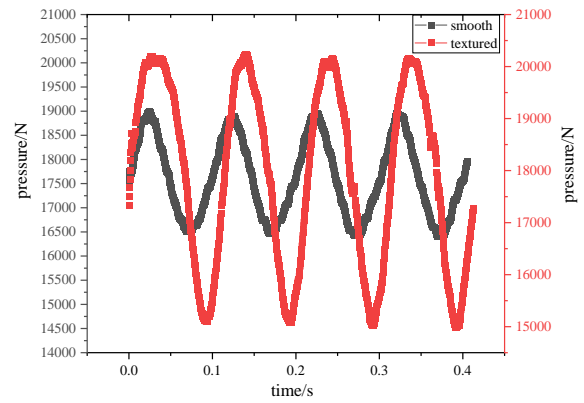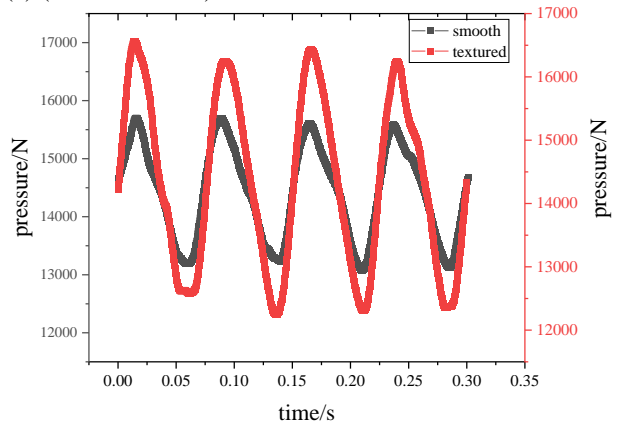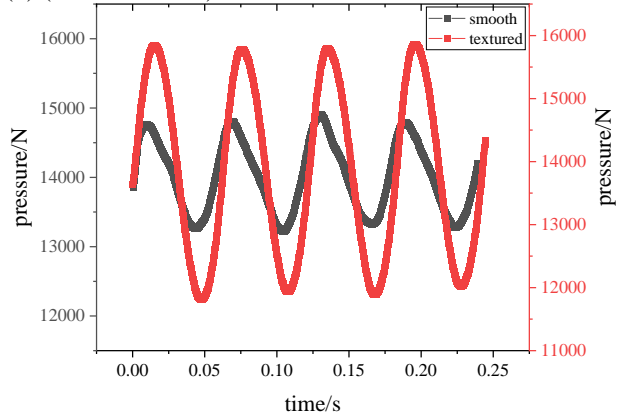
the graph, it can be seen that the pressure periodic changes over time. With increasing of rotational speed, the peak water film pressure shows a decreasing trend. At the same speed, the optimized bearing shows a rise in both the peak and valley values of pressure compared to the peak and valley values of the smooth bearing. This shows that the fluid dynamic pressure effect is greater in the optimized textured bearing than in the smooth bearing.

5. CONCLUSION

The focus of the article is on the lubrication performance and optimization design of textured water-lubricated journal bearings. The main conclusions are summarized as follows:

A lubrication model of a textured two-dimensional parallel friction pair is developed to investigate the effect of structural parameters of the texture on the lubrication performance of the friction pair. The research indicates the following: (1) With increasing of h/d, the maximum positive pressure gradually falls. With increasing of d/L, the maximum positive pressure rises while the area of the negative pressure zone falls, and the load-carrying capacity rises. Moreover, with increasing h/h_0, there is an optimal value that maximizes the load-carrying capacity. (2) A smaller texture width will inhibit the occurrence of liquid film cavitation. With an increasing texture width, the degree of cavitation gradually rises and stabilizes. With the texture depth getting larger, the micro dynamic pressure effect is enhanced, and the liquid film pressure rises.

Then, a multi-objective optimization method combining the response surface and NSGA-II is used to optimize the textured journal bearings. Furthermore, the optimization results are verified by experiments. The conclusions are summarized as follows: (3) The optimized parameters of the textured journal bearing are obtained via NSGA- II. The load-carrying capacity of the optimized bearing rises and the friction falls. (4) Through frictional wear tests and water film pressure tests, it turned out that the optimized texture parameters can effectively diminish the friction and wear volume, and the optimized textured bearing hydrodynamic pressure effect is enhanced at the same speed.

In this paper, the lubrication performance of journal bearings is analyzed from the point of view of texture structural parameters, besides ， the load-carrying capacity and friction performance of textured journal bearings are optimized with multiple objectives. The results and conclusions of the study provide some references for the further development of surface texture optimization and design.

6. LIMITATIONS

Although the research work in this paper has achieved some results, due to the limitations of texture processing, the experiment in this paper converts the textured water-lubricated bearings into parallel friction pairs for friction and wear test. With the further development of texture processing technology, the lubrication performance of optimized journal bearings at different speeds can be better verified, and the effect of texture parameters on lubrication performance can be further verified.

Moreover, due to the complexity of the large number of design parameters, textures can be harmful if inappropriate values are chosen. Choosing the right texture size is important for the popularization and application of surface texture technology.

CONFLICT OF INTEREST

The authors declare that they have no known competing financial interests or personal relationships that could have appeared to influence the work reported in this paper.

AUTHORS CONTRIBUTION

Qiang Li: Conceptualization, Writing – review & editing. **Yu Wang:** Conceptualization, Validation, Data curation, Formal analysis, Writing – review & editing. **Xingyang Li:** Validation, Data curation, Investigation. **Xiuwei Li:** Investigation, Conceptualization. **Guokun Zhang:** Investigation. **Yujing Du:** Conceptualization, Writing – review & editing. **Weiwei Xu:** Validation.

REFERENCES

ANSYS. (2011). *Ansys Fluent theory guide*. Monograph. Canonsburg, USA.

Brizmer, V., Kligerman, Y., & Etsion, I. (2003). A laser surface textured parallel thrust bearing. *Tribology Transactions*, *46*(3), 397-403. https://doi.org/10.1080/10402000308982643

Deb, K., Pratap, A., Agarwal, S., & Meyarivan, T. (2002) A fast and elitist multi-objective genetic algorithm: NSGA-I. *IEEE Transactions on Evolutionary Computation*, *6*(2), 182-197. https://doi.org/10.1109/4235.996017

Dobrica, M. B., Fillon, M., & Pascovici, M. D. (2010). Optimizing surface texture for hydrodynamic lubricated contacts using a mass-conserving numerical approach. *Proceedings of the Institution of Mechanical Engineers. Part J: Engineering Tribology,* *224*(8), 737-750. https://journals.sagepub.com/doi/10.1243/13506501 JET673

Etsion, I., Halperin, G., Brizmer, V. & Kligerman, Y. (2004). Experimental investigation of laser surface textured parallel thrust bearings. *Tribology. Letters*, *17*(2), 295-300. https://doi.org/10.1023/B:TRIL.0000032467.88800. 59

Gao, G., Yin, Z., Jiang, D., & Zhang, X. (2014). Numerical analysis of plain journal bearing under hydrodynamic lubrication by water. *Tribology International*, *75*, 31-38. https://doi.org/10.1016/j.triboint.2014.03.009

Gherca, A. R., Maspeyrot, P., Hajjam, M., & Fatu, A. (2013). Influence of texture geometry on the hydrodynamic performances of parallel bearings. *Tribology Transactions*, *56*(3), 321-332. https://doi.org/10.1080/10402004.2012.752550

Gropper, D., Wang, L., & Harvey, T. J. (2016). Hydrodynamic lubrication of textured surfaces: a review of modeling techniques and key findings. *Tribology International*, *94*, 509-529. https://doi.org/10.1016/j.triboint.2015.10.009

Guo, L. (2007). Progress of research on water lubricated bearings. *Precise Manufacturing & Automation,* (1), 6-9, 26. https://doi.org/10.3969/j.issn.1009-962X.2007.01.003

Guo, S. H. (2023). *Theoretical analysis and experimental studay on the influence of surface micro texture on lubrication characteristics of journal bearing* [Doctoral dissertation, Shandong University of Science and Technology].

Ilka, R., Alinejad-Beromi. Y., & Yaghobi, H. (2018) Cogging torque reduction of permanent magnet synchronous motor using multi-objective optimization. *Mathematics and Computers in Simulation*, *153*, 83-95. https://doi.org/10.1016/j.matcom.2018.05.018

Ji, J. H., Deng, Z. W., Chen, T. Y., Fang, L. N., & Fu, Y. H. (2020). Analysis of hydrodynamic lubrication of partially textured infinitely long tilting pad thrust bearing. *Surface Technology*, *50*(2), 246-253. https://doi.org/10.16490/j.cnki.issn.1001-3660.2021.02.025

Kango, S., Singh, D., & Sharma, R. K. (2012). Numerical investigation on the influence of surface texture on the performance of hydrodynamic journal bearing. *Meccanica*, *47*(2), 469-482. https://doi.org/10.1007/s11012-011-9460-y

Li, Z. Y., Xiong, X. H., &Wu, J. M. (2004). Introduction to common numerical methods in computational fluid mechanics. *Guangdong Shipbuilding*, *3*, 5-8.

Mallya, R., Shenoy, S. B., & Pai, R. (2016). Static characteristics of misaligned multiple axial groove water-lubricated bearing in the turbulent regime. *Proceedings of the Institution of Mechanical Engineers Part J Journal of Engineering Tribology, 231*(3), 385-398. https://doi.org/10.1177/1350650116657757

Marian, V. G., Gabriel, D., Knoll, G., & Filippone, S. (2011). Theoretical and experimental analysis of a laser textured thrust bearing. *Tribology. Letters*, *44*(3), 335-343. https://doi.org/10.1007/s11249-011-9857-8

Marian, V. G., Kilian, M., & Scholz, W. (2007). Theoretical and experimental analysis of a partially textured thrust bearing with square dimples. *Proceedings of the Institution of Mechanical Engineers Part J Journal of Engineering Tribology*, *221*(7), 771-778. https://doi.org/10.1243/13506501JET292

Qiao, J. S., Zhou, G. W., Pu, W., Li, R., He, M. (2022). Coupling analysis of turbulent and mixed lubrication of water-lubricated rubber bearings. *Tribology International,* *172*, 107644. https://doi.org/10.1016/j.triboint.2022.107644.

Rao, T. V. V. L. N., Rani, A. M. A., Nagarajan, T., & Hashim, F. M. (2014). Analysis of couple stress fluid lubricated partially textured slip slider and journal bearing using narrow groove theory. *Tribology International*, *69*, 1-9. https://doi.org/10.1016/j.triboint.2013.08.006

Savio, D., Falk, K., & Moseler, M. (2018). Slipping domains in water-lubricated microsystems for improved load support. *Tribology International*, (120), 269-279. https://doi.org/10.1016/j.triboint.2017.12.030

Tan, K. H. R. T. (2007). *Modelling of fluid flow in multiple axial groove water lubricated bearings using computational fluid dynamics* [Masters thesis, Queensland University of Technology].

Uddin, M. S., Ibatan, T., & Shankar, S. (2017). Influence of surface texture shape, geometry and orientation on hydrodynamic lubrication performance of plane-to-plane slider surfaces. *Lubrication Science*, *29*(3), 153- 181. https://doi.org/10.1002/ls.1362

Wang, X., Kato, K., Adachi, K., & Aizawa, K. (2003). Loads carrying capacity map for the surface texture design of SiC thrust bearing sliding in water. *Tribology International*, *36*(3), 189-197. https://doi.org/10.1016/S0301-679X(02)00145-7

Wang, X., Shi. L., Dai, Q., Huang, W., Wang, X. L. (2018) Multi-objective optimization on dimple shapes for gas face seal. *Tribology International*,*123*, 216-223. https://doi.org/10.1016/j.triboint.2018.03.011

Wang, Y. J. (2021). *Hydrodynamic lubrication mechanism and multi-objective driven optimization design of textured friction contacts* [Master thesis, China University of Petroleum].

Wang, Y. Z., Yin, Z. W., Jiang, D, Gao, G. Y., Zhang, X. L. (2016). Study of the lubrication performance of water-lubricated journal bearings with CFD and FSI method. *Industrial Lubrication and Tribology, 68*(3), 341-348. https://doi.org/10.1108/ILT-04-2015-0053/full/html

Wu, Z., Guo, Z., & Yuan, C. (2020). Insight into water lubrication performance of polyetheretherketone. *Journal of Applied Polymer Science*, *138*(4), 49701. https://doi.org/10.1002/app.49701

Xiang, H. (2017). EHL analysis of textured fractal surface based on thermal effect. *Surface Technology*, *46*(12),

141-146. https://doi.org/10.16490/j.cnki.issn.1001-3660.2017.12.023

Xie, Z. L., Jiao, J., Yang, K., et al. (2023). A state-of-art review on the water-lubricated bearing. *Tribology International, 180*, 108276. https://doi.org/10.1016/j.triboint.2023.108276

Xi-Jun, H., Hong-Shan, X. U., Ya-Lin, C., Xuan, X., Shang, X. U., & Cheng, W. (2018). Numerical analysis on lubrication performance of laser micro-textured roller bearings. *Surface Technology*, *47*(3), 36-41. https://doi.org/10.16490/j.cnki.issn.1001-3660.2018.03.006

Ye, X., Wang, J., Zhang, D., Hu, J., & Feng, Y. (2014). The dynamic characteristic analysis of the water lubricated bearing-rotor system in seawater desalination pump. *Advances in Mechanical Engineering*, 356578-356578. https://doi.org/10.1155/2014/356578

Ye, X., Wang, J., Zhang, D., Hu, L., & She, X. (2016). Experimental research of journal orbit for water-lubricated bearing. *Mathematical Problems in Engineering*, 8361596. https://doi.org/10.1155/2016/8361596

Zhang, S. (2020). *Liquid film cavitation mechanism and dynamic characteristics of journal bearings* [Master thesis, China University of Petroleum].

Zhao, Y. F., Yang, J. X., & Mao, Y. Z. (2020). Effect of texture arrangement on friction and wear characteristics of sliding bearings. *Bearing*, *9*, 33-37. https://doi.org/10.19533/j.issn1000-3762.2020.09.008

Zhou, G. W. (2013). *Mixed lubrication analysis and dynamic performance optimization of water lubricated rubber alloy bearings* [Doctoral dissertation, Chongqing University].

Zou, L., Liu Z. L., Kao, J. C. M., & Sung, W. P. (2016). Influence of stern shaft inclination on the cooling performance of water-lubricated bearing. *China Shiprepair*, *63*, 02024. https://doi.org/10.1051/matecconf/20166302024